AUTONOMOUS HORIZON-BASED ASTEROID NAVIGATION WITH OBSERVABILITY ENHANCING MANEUVERS

Aditya A. Anibha[1*] and Kenshiro Oguri[2]; [1]Undergraduate Student, [2]Assistant Professor; School of Aeronautics and Astronautics, Purdue University, West Lafayette, Indiana, 47906; [1*]aanibha@purdue.edu [2*]koguri@purdue.edu

Abstract. *Asteroid exploration is a pertinent challenge due to the varying complexity of their dynamical environments, shape and communication delays due to distance. Thus, autonomous navigation methods are continually being developed and improved in current research to enable their safe exploration. These methods often involve using horizon-based Optical Navigation (OpNav) to determine the spacecraft's location, which is reliant on the visibility of the horizon. It is critical to ensure the reliability of this measurement such that the spacecraft may maintain an accurate state estimate throughout its mission. This paper presents an algorithm that generates control maneuvers for spacecraft to follow trajectories that allow continuously usable optical measurements to maintain system observability for safe navigation. This algorithm improves upon existing asteroid navigation capabilities by allowing the safe and robust autonomous targeting of various trajectories and orbits at a wide range of distances within optical measurement range. It is adaptable to different asteroid scenarios. Overall, the approach develops an all-encompassing system that simulates the asteroid dynamics, synthetic image generation, edge detection, horizon-based OpNav, filtering and observability-enhancing control.*

1 Introduction. Asteroid exploration has gained significant interest in recent times, driven by scientific research, resource utilization, and planetary defense purposes. Successful missions, such as *Hayabusa2* to 162173 Ryugu and *OSIRIS-REx* to 101955 Bennu, have provided valuable insights into the composition and structure of these small bodies.[1,2] However, both missions required extensive observation periods to safely navigate the uncertain and weak gravitational environments of their respective targets. For example, *OSIRIS-REx* spent nearly a year mapping Bennu before attempting proximity operations,[3] while *Hayabusa2* similarly mapped Ryugu for months.[4] In addition to these missions, the *DART* and *Lucy* missions also emphasize the need for detailed pre-mission observations to ensure safe proximity operations.[5,6] These missions highlight the need for improvements in autonomous OpNav to reduce the reliance on long observation periods or human-in-the-loop methods to improve mission efficiency and reliability.

OpNav (OpNav) has become a preferred method for space missions due to its reliability, accuracy, and accessibility, particularly when navigating larger spherical bodies like the Moon or Mars.[7] OpNav relies on visual images of celestial bodies, allowing spacecraft to determine their position by analyzing surface features or horizons. Some types of OpNav include surface feature tracking, Line Of Sight (LOS),[8] Central and Apparent Diameter (CAD),[9] Lidar-based[10,11] and Pole-from-Silhouette, Shape-from-Silhouette or Localization-from-Silhouette[12] methods.

In the case of *Hayabusa2*, both human-in-the-loop and autonomous OpNav is used extensively throughout the mission, from approach to landing and sample collection phases at asteroid 162173 Ryugu. The spacecraft employed a series of optical images captured by its onboard OpNav Camera (ONC) to estimate its position and velocity relative to the asteroid's surface. This information is crucial for accurately guiding the spacecraft during its low-altitude descents and surface interactions. In addition, OpNav is used during the mission's descent to provide detailed images of Ryugu's surface, enabling the mission team to select safe landing sites. The mission relied heavily on OpNav for proximity operations, including final descent and collection maneuvers, illustrating its importance in achieving mission success. Additionally, it also used a marker system for accurate autonomous operation in close proximity to the asteroid.[13]

Similarly, the *OSIRIS-REx* mission to asteroid 101955 Bennu also utilized human-in-the-loop OpNav during its approach, orbital phases, and sample collection. The spacecraft's onboard navigation system analyzed optical images captured by its navigation camera to determine its position relative to Bennu, particularly during its low-altitude maneuvers. This data allowed *OSIRIS-REx* to navigate Bennu's complex gravitational field, helping it to select sample collection sites and safely perform touch-and-go operations. The OpNav system provided real-time data during the mission's critical phases, including orbital insertion, detailed surface mapping, and final sample collection. Throughout the mission, OpNav proved invaluable, particularly in guiding the spacecraft during autonomous operations when Earth-based communication delays are too long for manual intervention.[14]

Natural feature tracking OpNav is computationally expensive and may not be effective at large distances or near the dark side, while using a physical marker method requires a close proximity to the asteroid. LOS is useful due to its ease of use and applicability at large distance, but at the cost of accuracy without radial range information. The newer silhouette methods offer promising accuracy and determine asteroid pole and shape in addition to localization, but may be limited

by computation time. More advanced methods of applying OpNav in the asteroid navigation context are continually being developed to enhance its performance using innovative techniques. 15 introduces an approach to optimize the spacecraft's orbit during the approach phase by enhancing OpNav observability using the Fisher Information Matrix (FIM). While this method significantly improves measurement reliability, it is still challenged by uncertainties due to the asteroid's irregular surface and dynamic environment, which could introduce errors. Additionally, the optimization process is too time and computation costly, thus posing a challenge for its onboard application. In another work,[16] the authors develop real-time image processing techniques for OpNav around binary asteroids, which use data-driven approaches to enhance the accuracy of navigation. However, the computational demand for processing large datasets in real-time presents a challenge, potentially limiting onboard resources. 17 presents an observability-based navigation strategy that combines optical and radiometric measurements to improve navigation during the asteroid approach phase. The spacecraft configuration is optimized to enhance the measurement and state estimation accuracy. However, this is only applicable to multi-spacecraft formations.

Another specific subset of OpNav involves the horizon-based method. Unlike the other aforementioned methods, horizon-based OpNav measures the apparent horizon of the celestial body to determine the spacecraft's position and orientation, making it effective at a wide range of distances and lighting conditions.[18] Furthermore, it is computationally efficient and feasible for real-time autonomous application. Horizon-based OpNav has yet to be fully utilized in asteroid missions, but its proven accuracy and reliability in spherical-body missions suggest it could be adapted to advance asteroid navigation capabilities. By using the asteroid's horizon rather than relying on surface features, horizon-based OpNav could ensure continuous and accurate navigation while expanding the usable range and angles, even in regions where surface visibility is limited, such as near the dark side. If successfully adapted for asteroid missions, it could help improve spacecraft autonomy, early mission approach time efficiencies, and reduce the need for manual interventions during critical mission phases. However, it is inaccurate when observing from an angle too far near the dark side of a target body when no horizon is detectable.

Therefore, there is a need to develop a computationally efficient, autonomous, robust and accurate OpNav and control algorithm. Ideally, this algorithm should function at a wide range of distances and angles while accounting for poor observability regions to ensure continuous and safe operation. This research proposes a novel solution: the development of a path-constrained Lyapunov controller that enhances optical observability during asteroid missions using the horizon-based method. Lyapunov control has been explored for application in the asteroid mission context, however the focus has been on orbit-attitude control and hovering operations.[19,20] This new proposed controller is dedicated to the improvement of the OpNav measurement method and ensures that the spacecraft avoids regions with poor visibility by adjusting its trajectory in real-time. This approach allows for continuous and reliable optical measurements, even near the dark side of the asteroid, thereby enhancing the overall safety and robustness of autonomous asteroid navigation.

The core technical approach of this paper involves deriving a Lyapunov controller that utilizes artificial potential functions to maintain a path with optimal observability. Additionally, we developed a synthetic asteroid image generation tool to simulate varying lighting conditions and test the performance of horizon-based OpNav in different scenarios. These simulations allow us to identify the limitations of existing OpNav methods, which then serve as inputs to our controller design. The proposed controller is tested in realistic mission scenarios, including orbit maintenance and approach for asteroid capture, with state estimation handled through the use of an Extended Kalman Filter (EKF). The performance of the controller is evaluated using Monte Carlo simulations to ensure robustness across various mission profiles. A schematic displaying the flow of the algorithm is shown in Fig. 1

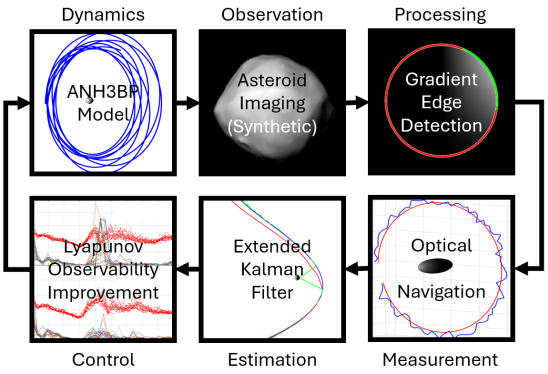

Figure 1. Overall Algorithm Schematic

The remainder of this paper is structured as follows. First, we discuss the dynamics model, horizon-based OpNav, and EKF, which form the foundation of our navigation system. Next, we describe the asteroid image generation technique and the edge detection methods used to test OpNav and analyze its limitations. Following this, we present the novel contribution of the observability-enhancing Lyapunov controller. Finally, we demonstrate the controller's effectiveness through analysis of OpNav and EKF performance, validated using Monte Carlo simulations under realistic mission

conditions.

2 Background and Preliminaries.

2.1 Dynamics. Let $\boldsymbol{x}$ be the state of our system. Thus, our generic equation of motion is expressed as follows:

$$\dot{\boldsymbol{x}} = \boldsymbol{f}_0(\boldsymbol{x}, t) + B\boldsymbol{u} \tag{1}$$

Where $\boldsymbol{f}_0(\boldsymbol{x}, t)$ represents the natural orbital dynamics, B is the control matrix that maps any control input or perturbing acceleration $\boldsymbol{u}$ to the state.

The motion of a spacecraft near primitive celestial bodies, such as asteroids, is influenced by several forces, including the gravitational pull of the body itself and the Sun, as well as Solar Radiation Pressure (SRP). The equations governing this motion are encapsulated in the Augmented Normalized Hill Three-Body Problem (ANH3BP), which provides a normalized framework accounting for these forces in a rotating reference frame.

This Hill frame is defined with the x-axis pointing from the Sun to the asteroid, the z-axis pointing toward the angular velocity of the asteroid, and the y-axis completing the frame.

The spacecraft's normalized position and velocity are denoted by $r = [x, y, z]$ and $v = [\dot{x}, \dot{y}, \dot{z}]$ respectively, within this frame where $\dot{r}$ and $\dot{v}$ are their time derivatives. The dynamical system is non-dimensionalized with the unit length $(\mu/\mu_{\text{Sun}})^{1/3}R$ and unit time $1/N$ using the gravitational parameter of the primitive body μ and the Sun μ_{Sun}, the distance between the Sun and the primitive body R and the mean motion of the primary orbits, $N = \sqrt{(\mu_{\text{Sun}}/R^3)}$. The equations of motion for the ANH3BP are:[21]

$$\begin{aligned} \ddot{x} &= 2\dot{y} + 3x - x/\|\mathbf{r}\|^3 + \beta \\ \ddot{y} &= -2\dot{x} - y/\|\mathbf{r}\|^3 \\ \ddot{z} &= -z - z/\|\mathbf{r}\|^3, \end{aligned} \tag{2}$$

The non-dimensional acceleration due to SRP is represented by β and calculated as follows:

$$\beta = \left(\frac{G_1}{(m/A)R^2}\right)\left(\frac{1}{N}\right)^2\left(\left(\frac{\mu}{\mu_{\text{Sun}}}\right)^{1/3}R\right)^{-1} = \frac{G_1}{(m/A)\mu_{\text{Sun}}^{2/3}\mu^{1/3}} \tag{3}$$

Where G_1 is the solar flux constant and m/A is the spacecraft mass-to-area ratio.

This may be rewritten in the following state space form:

$$\begin{aligned} \boldsymbol{f}_0(\boldsymbol{x}, t) &= \begin{bmatrix} \boldsymbol{v} \\ 2\dot{y} + 3x - \frac{x}{\|\mathbf{r}\|^3} + \beta \\ -2\dot{x} - \frac{y}{\|\mathbf{r}\|^3} \\ -z\frac{-z}{\|\mathbf{r}\|^3} \end{bmatrix} \\ B &= \begin{bmatrix} 0_{3\times3} \\ I_{3\times3} \end{bmatrix} \end{aligned} \tag{4}$$

It is important to note that this model involves approximation due to the assumptions that the asteroid is in a circular orbit and SRP acceleration is constant.

An important defining condition for an orbit to be bounded around the primitive body within this model is the maximum semi major axis, defined as follows for a frozen terminator orbit:[22]

$$a_{\max} = \frac{\sqrt{3}}{4}\sqrt{\frac{\mu(m/A)}{G_1}}R \tag{5}$$

Where $a_{\max}$ is the maximum semi major axis of the orbit beyond which escape occurs. A random value for the semi major axis can be selected between the range of the maximum stable value and the mean radius of the asteroid when testing for orbital testcases. This is used as a reference value to define the numerical simulations in Sections 5 and 6.

An alternate representation of this dynamics can be formulated using Milankovitch elements. To model the ANH3BP in Milankovitch form, the Gauss planetary equation form is used with added SRP and solar gravity perturbations as shown:

$$\begin{aligned} \boldsymbol{f}_0(\boldsymbol{x}) &= \begin{bmatrix} 0 \\ 0 \\ 0 \\ 0 \\ 0 \\ \frac{h}{r^2} \end{bmatrix} + B(\boldsymbol{a}_{\text{SRP}} + \boldsymbol{a}_{\text{Solar}}) \\ \boldsymbol{x} &= \begin{bmatrix} \boldsymbol{h} \\ \boldsymbol{e} \\ L \end{bmatrix} \\ B &= \frac{1}{h}\begin{bmatrix} \tilde{\boldsymbol{r}} \\ \frac{1}{\mu}(\tilde{\boldsymbol{v}}\tilde{\boldsymbol{r}} - \tilde{\boldsymbol{h}}) \\ \frac{\hat{\boldsymbol{z}}\cdot\boldsymbol{r}}{h(h+\hat{\boldsymbol{z}}\cdot\boldsymbol{h})}\boldsymbol{h} \end{bmatrix} \\ \boldsymbol{a}_{SRP} &= \begin{bmatrix} \beta \\ 0 \\ 0 \end{bmatrix} \\ \boldsymbol{a}_{\text{Solar}} &= -\mu\left(\frac{r - r_{\text{asteroid}}}{\|r - r_{\text{asteroid}}\|_2^3} + \frac{r_{\text{asteroid}}}{\|r_{\text{asteroid}}\|_2^3}\right) \end{aligned} \tag{6}$$

Where $\boldsymbol{h}$ is the angular momentum vector, and h is its magnitude.

2.2 Horizon-based OpNav. Moving on to the measurement implementation, Christian's OpNav (OpNav) algorithm[18] is utilized. It is a computing time efficient and accurate method to calculate the position of an observer from a target body as it directly computes from the edge detected horizon points rather than using curve fitting. The observations for the EKF and the simulation are derived from this OpNav process. The Christian-Robinson OpNav pseudocode can be depicted as in Algorithm 1.

Algorithm 1 Pseudocode for the Christian-Robinson OpNav algorithm[18]

procedure r_C = OpNav($(\vec{u}_i')_{i=1}^n, K^{-1}, T_C^P, a, b, c$)
  Compute $D = \text{diag}[1/a, 1/b, 1/c]$
  Compute $R = DT_C^P K^{-1}$
  for $i = 1$ to n **do**
    $\vec{x}_i' = R\vec{u}_i$
    $s_i' = \vec{x}_i'/\|\vec{x}_i'\|$
  end for
  Construct H from $\{s_i'\}_{i=1}^n$
  Compute TLS solution for n
  Compute $T_C^P = (T_C^P)^\top$
  Compute $D^{-1} = \text{diag}[a, b, c]$
  Compute r_C
end procedure
return r_C

The inputs include the pixel coordinates of all the detected points in the camera frame, the inverse camera calibration matrix, the attitude transformation matrix between the parent body to the camera, and the triaxial parameters of the shape of the target body. The inverse camera matrix is defined as follows:

$$\boldsymbol{K}^{-1} = \begin{bmatrix} \frac{1}{d_x} & \frac{-\alpha}{d_x d_y} & \frac{\alpha v_p - d_y u_p}{d_x d_y} \\ 0 & \frac{1}{d_y} & \frac{-v_p}{d_y} \\ 0 & 0 & 1 \end{bmatrix} \tag{7}$$

Where d_x and d_y are the unit pixel density in the x and y directions respectively, f is the focal length, $u_p = S/2$ and $v_p = S/2$ are the principal point coordinates and α is the skew of the pixels. S is the image size measured in pixels. The focal length can be calculated as follows:

$$f = \frac{(S/2)}{\tan(\theta/2)} \tag{8}$$

Where θ is the is the camera field of view angle.

Since this is a case of known attitude, the magnitude of the position measurement returned by the OpNav algorithm is transformed into the ANH3BP coordinate frame using the current attitude.

Since we require the measurement covariance to use this method with an EKF, The analytical form is shown in Algorithm 2.

2.3 Extended Kalman Filter. An Extended Kalman Filter (EKF) is used to perform the state estimation using the OpNav measurements. Testing the EKF's performance across a range of operational scenarios help to establish the algorithm's robustness and identify areas for enhancement. First, some key assumptions include the satellite's ability to continuously observe the asteroid with its optical camera via nadir pointing (i.e., the camera is always oriented to point towards the center of the target body), the attitude of the spacecraft relative to the asteroid is always known, the asteroid shape is known, and the availability of initial state estimates with inherent uncertainties. These assumptions are made to simplify the problem and focus on estimating the position. Constraints involve the limitations of the camera's resolution and the accuracy of onboard sensors, the maximum semi major axis for a stable orbit in this system, as well as the computational complexity of generating and processing synthetic observation images in real-time. The EKF is defined in Cartesian form, and algorithm used is as follows.

Algorithm 2 OpNav Analytical Covariance Algorithm[23]

procedure OpNav_COV(D, $(\vec{u}_i')_{i=1}^n$, σ_{pix}, d_x)
  Compute r_C and n using Algorithm 1
  Form covariance of the horizon measurements, R_s
  for each $\vec{u}_i'$ **do**
    Compute the partial, J_i
    Compute the variance of each residual, $\sigma_{v_i}^2$
    Construct residual covariance, R_y
  end for
  Compute least-square covariance, P_n
  Compute F, the partial derivative of r_C wrt n
  Calculate OpNav Covariance, P_r
end procedure
return P_r

$$\begin{aligned} \hat{\boldsymbol{x}}_{k|k-1} &= f\left(\hat{\boldsymbol{x}}_{k-1|k-1}, \boldsymbol{u}_{k-1}\right) \\ \boldsymbol{P}_{k|k-1} &= \boldsymbol{F}_k \boldsymbol{P}_{k-1|k-1} \boldsymbol{F}_k^\top + \boldsymbol{Q}_{k-1} \\ \tilde{\boldsymbol{y}}_k &= \boldsymbol{z}_k - h\left(\hat{\boldsymbol{x}}_{k|k-1}\right) \\ \boldsymbol{S}_k &= \boldsymbol{H}_k \boldsymbol{P}_{k|k-1} \boldsymbol{H}_k^\top + \boldsymbol{R}_k \\ \boldsymbol{K}_k &= \boldsymbol{P}_{k|k-1} \boldsymbol{H}_k^\top \boldsymbol{S}_k^{-1} \\ \hat{\boldsymbol{x}}_{k|k} &= \hat{\boldsymbol{x}}_{k|k-1} + \boldsymbol{K}_k \tilde{\boldsymbol{y}}_k \\ \boldsymbol{P}_{k|k} &= \left(\boldsymbol{I} - \boldsymbol{K}_k \boldsymbol{H}_k\right) \boldsymbol{P}_{k|k-1} \end{aligned} \tag{9}$$

Where the state space matrix in Cartesian form is:

$$\boldsymbol{x} = \begin{bmatrix} x & y & z & \dot{x} & \dot{y} & \dot{z} \end{bmatrix}^\top \tag{10}$$

The state transition matrix is calculated as the jacobian of the equations of motion of the ANH3BP from Equation 1. In the Cartesian case, we get the following jacobian:

$$J = \begin{bmatrix} 0 & 0 & 0 & 1 & 0 & 0 & 0 \\ 0 & 0 & 0 & 0 & 1 & 0 & 0 \\ 0 & 0 & 0 & 0 & 0 & 1 & 0 \\ 3 - \frac{1}{r^3} + \frac{3x^2}{r^5} & \frac{3xy}{r^5} & \frac{3xz}{r^5} & 0 & 2 & 0 & 0 \\ \frac{3yx}{r^5} & -\frac{1}{r^3} + \frac{3y^2}{r^5} & \frac{3yz}{r^5} & -2 & 0 & 0 & 0 \\ \frac{3zx}{r^5} & \frac{3zy}{r^5} & -1 - \frac{1}{r^3} + \frac{3z^2}{r^5} & 0 & 0 & 0 & 0 \\ 0 & 0 & 0 & 0 & 0 & 0 & 1 \end{bmatrix} \tag{11}$$

where $r = \sqrt{x^2 + y^2 + z^2}$.
The OpNav measurement returns values in the format

$$\boldsymbol{z} = \begin{bmatrix} r_{C,x} & r_{C,y} & r_{C,z} \end{bmatrix}^\top \tag{12}$$

The observation matrix H is:

$$H = \begin{bmatrix} 1 & 0 & 0 & 0 & 0 & 0 \\ 0 & 1 & 0 & 0 & 0 & 0 \\ 0 & 0 & 1 & 0 & 0 & 0 \end{bmatrix} \tag{13}$$

2.4 Lyapunov Control. Lyapunov control is a method that ensures dynamical system stability through the development of Lyapunov functions in a nonlinear feedback control case. It is particularly useful as it allows for the creation of an analytical controller with light computational cost and is easy to implement. Furthermore, it is possible to incorporate path constraints using artificial penalty functions. However, the lyapunov controller is not guaranteed the path constraint and requires gain or penalty weight and sharpness tuning. It may also not return an optimal solution, but its efficiency and satisfactory performance prove it to be a good option for this research. A Lyapunov function[24] is a scalar continuous function $V(x)$ that is locally positive or negative definite about a reference state x_r of an autonomous system $\dot{\boldsymbol{x}} = \boldsymbol{f}(\boldsymbol{x})$.

In spacecraft control, Lyapunov functions can be designed to guide the spacecraft's state toward a desired configuration, such as a stable orbit, attitude or particular rendezvous point.[25] By defining an appropriate Lyapunov function for a spacecraft's position and velocity, the system can be controlled to remain stable under perturbations, such as SRP or irregular gravitation in the case of an asteroid. Control inputs are applied to approach a desired target state. These inputs are derived from the gradient of the Lyapunov function, ensuring that the spacecraft moves in a direction that reduces the overall system energy. The approach is to design a controller $\boldsymbol{u} = \boldsymbol{g}(\boldsymbol{y})$ such that $V(x)$ is a Lyapunov function.

3 Synthetic Image Generation Pipeline. The image generation is done using built-in matlab graphics tools. The procedure involved illuminating a white sphere, ellipsoid, or 3-dimensional mesh model of an asteroid against a black background with the mean radius of Bennu (or any sample asteroid) using an infinitely far away light source that is aligned to originate from the negative x-axis to represent a parallel ray light source like the Sun. Gaussian white noise is added to the image to add realistic complexity for the filter to process. Edge detection is executed by identifying high gradient magnitudes between pixels on the image, which is commonly where the lit limb edge meets blank space. The camera is then placed based on an input distance, azimuth and elevation as calculated prior. A few examples of generated images are shown in Fig. 2, followed by a stepwise summary of the MATLAB algorithm utilised for the synthetic image generation:

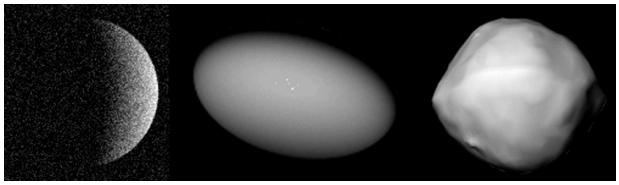

Figure 2. Example synthetic images of a half illuminated sphere (with noise), ellipsoid, and Bennu model at a distance of 5 radii

1. Generate either a sphere, ellipsoid or mesh scaled according to either the camera settings and distance, or an experimentally determined scale factor. With the OpNav settings used in this research, this is found experimentally to be 1.3065. This was found by visually comparing generated images with real images and verifying the OpNav measurement across a range of distances, then fitting an ideal scale factor to account for MATLAB's inherent figure environment scaling.

2. Create a figure with invisible, equal and tight axes and a black background. Plot the generated object as a surface with LineStyle set to none and a white colormap.

3. Set the view angle, camera position and roll according to the current spacecraft attitude.

4. Delete existing lights and replace them with a light set at an infinite distance to simulate the Sun. Use gouraud lighting and dull material for realistic surface and lighting conditions, with no ambient or specular reflection, a diffused reflection coefficient of 1 and a shininess coefficient of 10. These parameters were chosen as they produced the most visually accurate images compared to real examples.

5. Set the figure size and axis limits according to the image size, apply the camera's FOV setting to the axes camera view angle and set aspect ratios to be equal

6. Store the image as a frame, then convert it to an image and resize it to the calculated image size in pixels. Convert the image to grayscale and output it for further processing.

To detect the horizon points from the generated synthetic images, we use a gradient-based approach. First, calculate the gradient of the image matrix and find the gradient magnitude at each pixel. Next, find the maximum gradient magnitude across the entire image. Then, multiply this value by 0.7 to define a minimum gradient threshold and find the pixel coordinates of all points that have a gradient magnitude above it. These are the desired horizon points. The value of 0.7 was chosen due to offering the best performance after some experimental testing. To avoid detection of random noisy

pixels, set the absolute minimum gradient threshold to 0.1, which was determined experimentally by finding an appropriate threshold above the maximum gradient in dark-side lighting conditions, but below the maximum gradient of regular lighting conditions.

4 Observability Enhancing Controller Design. The goal is to design a controller that generates a controlled trajectory along which the view of the asteroid is always in favorable lighting condition. A Lyapunov controller is sufficient for this application, and both easy to implement as well as computationally efficient. The objective is to develop a Lyapunov controller that avoids certain regions where the OpNav algorithm performs poorly. These poor observability regions have been characterized experimentally in Section 5.

We have designed two types of Lyapunov controllers, where the first controller aims to target and control the spacecraft towards the asteroid, starting at rest from a distance at the maximum observability range of OpNav and the second controller transfers to a certain small frozen terminator orbit around the asteroid. The motivation behind developing two distinct controllers is that they both provide benefits for different situations. The first controller uses a Cartesian form since it is easy to tune feedback gain, guarantees convergence without a control bound and better performing to target a specific target rendezvous point. This is ideal for approach, flyby or capture scenarios. The second controller uses Milankovitch elements as this is better to control and transfer between orbits when already in close proximity to the body and there is no specific target rendezvous point, but rather a target orbit. The orbit maintenance scenario uses the second controller, while the approach and capture scenario uses both to form a two-stage switching Lyapunov controller.

Both controllers have the same state path constraints, which have been experimentally determined by testing the OpNav algorithm's performance across varying distance and angle.

The constraints are listed as follows:

- Minimum radius on position of $2R_{\text{asteroid}}$
- Maximum radius on position of $25R_{\text{asteroid}}$
- Keep-out Cone with half-angle of 30 degrees along positive x-axis to avoid dark-side observations

where R_{asteroid} is the radius of the asteroid.

4.1 Controller 1 - Asteroid Approach Targeting. In this case, the intent is to ensure the spacecraft safely and successfully approaches the asteroid. Thus, we may use the origin, or gravitational center of the asteroid, as a fixed target state. This allows the spacecraft to modify its trajectory to exactly target the asteroid and account for perturbations, which is useful during the initial stages of a mission while approaching it from a distance. Using the system dynamics from Equation 3, the first step is to derive the error dynamics to provide a reference for the Lyapunov controller to reduce. This defines the error between the desired and current state of the spacecraft in terms of the dynamical system. We start by defining the state error $\delta\boldsymbol{x}$ as the difference between the true state $\boldsymbol{x}$ and the desired state $\boldsymbol{x}^*$. However, since the desired state is the origin of the system and forms a zero vector, it is omitted from the equation. The error dynamics are represented as the derivative of the state error.

$$\begin{aligned} \delta\boldsymbol{x} &= \boldsymbol{x} \\ \delta\dot{\boldsymbol{x}} &= \dot{\boldsymbol{x}} \end{aligned} \tag{14}$$

This can be rewritten in matrix form considering velocity, acceleration, and control elements.

$$\delta\dot{\boldsymbol{x}} = \begin{bmatrix} \boldsymbol{v} \\ \boldsymbol{a} + \boldsymbol{u} \end{bmatrix} \tag{15}$$

Now, we derive the controller by considering the candidate Lyapunov function as follows:

$$V = \frac{1}{2}\delta\boldsymbol{x}^\top K \delta\boldsymbol{x} \tag{16}$$

Where K must be a positive definite 6×6 matrix. It is therefore full rank and invertible. Take the derivative to find the Lyapunov rate:

$$\dot{V} = \frac{1}{2}\left(\delta\dot{\boldsymbol{x}}^\top K \delta\boldsymbol{x} + \delta\boldsymbol{x}^\top K \delta\dot{\boldsymbol{x}}\right) = \delta\boldsymbol{x}^\top K \delta\dot{\boldsymbol{x}} \tag{17}$$

The next step is to incorporate path constraints using artificial potential functions. To do this, the Lyapunov function and rate results need to be augmented by considering some additive potential function V_{P_i} from each penalty function, which we can define in the following form:

$$V_P = wV(\boldsymbol{x})P(g(\boldsymbol{x})) \tag{18}$$

Where w is the weight of the penalty, and P is the penalty function in terms of the path constraint $g(\boldsymbol{x}) \leq 0$ which must be negative at the target state and smooth everywhere. The penalty function should also be monotonically increasing in g for $g > 0$. For this, we define the penalty functions to be set to 0 when the constraint condition is not violated, and greater than 0 when it is. This can be represented as follows:

$$P(g)\begin{cases} > 0 & g > -\varepsilon \\ = 0 & g \leq -\varepsilon \end{cases} \tag{19}$$

Where ϵ may be defined to represent the point at which the constraint becomes applicable. We use the exponential form for all of our constraints since it is a smooth

and continuous function and therefore compatible in the Lyapunov context.

$$P_i(g_i) = e^{k_i g_i} \tag{20}$$

Where k is the sharpness parameter and is one of the variables that may be tuned. Now, we may add the three desired artificial potentials for each path constraint penalty as follows:

$$\hat{V} = V + V_{P_1} + V_{P_2} + V_{P_3} \tag{21}$$

Substituting in for the weights and penalty functions then taking the derivative, we find the augmented Lyapunov rate expression:

$$\dot{\hat{V}} = \dot{V}(1 + \sum \omega_i P_i) + V \sum \omega_i \dot{P}_i \tag{22}$$

Using this form, we attempt to derive a Lyapunov controller. For simplicity, we start by assuming a case with just one penalty function:

$$\hat{V} = V + V_P \tag{23}$$

Repeat the substitution of weights and penalty functions to get an expression for the augmented Lyapunov rate:

$$\dot{\hat{V}} = \dot{V}(1 + \omega P) + V\omega\dot{P} \tag{24}$$

Use the following chain rule properties to compute the derivatives of V and P:

$$\dot{V} = \frac{\mathrm{d}V}{\mathrm{d}\boldsymbol{x}} \frac{\mathrm{d}\boldsymbol{x}}{\mathrm{d}t} = (\delta\boldsymbol{x}^\top K)(f_0(\boldsymbol{x}, t) + B\boldsymbol{u}) \tag{25}$$

$$\dot{P} = \frac{\mathrm{d}P}{\mathrm{d}g} \frac{\mathrm{d}g}{\mathrm{d}\boldsymbol{x}} \frac{\mathrm{d}\boldsymbol{x}}{\mathrm{d}t} = \frac{\mathrm{d}P}{\mathrm{d}g} \frac{\mathrm{d}g}{\mathrm{d}\boldsymbol{x}} (f_0(\boldsymbol{x}, t) + B\boldsymbol{u}) \tag{26}$$

Additionally, to get the desired stabilizing controller, we then set the Lyapunov rate equal to a negative simple Lyapunov candidate function and algebraically solve for the control expression.

$$\dot{\hat{V}} = -\delta\boldsymbol{x}^\top Q \delta\boldsymbol{x} \tag{27}$$

Where Q is assumed to be of the form $I_{6\times6}$ and positive definite. We then equate the two expressions for the augmented Lyapunov rate and solve for the control u.

$$\delta\boldsymbol{x}^\top((1 + \omega P)K + \omega(\tfrac{1}{2}K\delta\boldsymbol{x})\tfrac{\mathrm{d}P}{\mathrm{d}g}\tfrac{\mathrm{d}g}{\mathrm{d}\boldsymbol{x}})(\boldsymbol{f}_0 + B\boldsymbol{u})) = -\delta\boldsymbol{x}^\top Q\delta\boldsymbol{x} \tag{28}$$

For compact expression, define the following:

$$L = ((1 + \omega P)K + \omega(\frac{1}{2}K\delta\boldsymbol{x})\frac{\mathrm{d}P}{\mathrm{d}g}\frac{\mathrm{d}g}{\mathrm{d}\boldsymbol{x}}) \tag{29}$$

This may be expanded to consider multiple penalty functions in the following form:

$$L = ((1 + \sum \omega_i \dot{P}_i)K + (\frac{1}{2}K\delta\boldsymbol{x})\sum \omega_i \frac{\mathrm{d}P_i}{\mathrm{d}g_i}\frac{\mathrm{d}g_i}{\mathrm{d}\boldsymbol{x}}) \tag{30}$$

Where L is a 6×6 matrix. It is assumed to be full rank and therefore invertible. Substitute back into the original equation.

$$B\boldsymbol{u} = -L^{-1}Q\delta\boldsymbol{x} - \boldsymbol{f}_0 \tag{31}$$

B is not square, therefore we use a pseudo-inverse to get the following final result for the controller:

$$\boldsymbol{u} = -(B^\top B)^{-1}B^\top(L^{-1}Q\delta\boldsymbol{x} - \boldsymbol{f}_0) \tag{32}$$

Now, we move on to defining our three penalty constraints in mathematical terms.

Start by deriving the minimum radius constraint using the parameters $r_{\min}$, weight ω_1 and sharpness k_1 to find the following formulation:

$$g_1(\boldsymbol{x}) = r_{\min}^2 - \boldsymbol{r}^2 = r_{\min}^2 - (x^2 + y^2 + z^2) \tag{33}$$

$$\frac{dg_1(\boldsymbol{x})}{d\boldsymbol{x}} = -2\boldsymbol{r} = \begin{bmatrix} -2x \\ -2y \\ -2z \\ 0_{3\times1} \end{bmatrix} \tag{34}$$

Repeat the process for the maximum radius constraint, $r_{\max}$ with the weight ω_2 and sharpness k_2.

$$g_2(\boldsymbol{x}) = \boldsymbol{r}^2 - r_{\max}^2 = (x^2 + y^2 + z^2) - r_{\max}^2 \tag{35}$$

$$\frac{dg_2(\boldsymbol{x})}{d\boldsymbol{x}} = 2\boldsymbol{r} = \begin{bmatrix} 2x \\ 2y \\ 2z \\ 0_{3\times1} \end{bmatrix} \tag{36}$$

Repeat the process for the cone constraint along x-axis with half angle α, weight ω_3 and sharpness k_3.

$$g_3(\boldsymbol{x}) = \frac{y^2 + z^2}{x^2} - \tan^2\alpha \tag{37}$$

$$\frac{dg_3(\boldsymbol{x})}{d\boldsymbol{x}} = \begin{bmatrix} \frac{-2(y^2+z^2)}{x^3} \\ \frac{2y}{x^2} \\ \frac{2z}{x^2} \\ 0_{3\times1} \end{bmatrix} \tag{38}$$

These penalty functions are then incorporated into the controller derived earlier to impose the path constraints.

4.2 Controller 2 - Frozen Terminator Orbit Transfer. For this controller, Milankovitch elements are used because they have no singularity and are better for orbital transfer maneuvers since it is possible to target a certain orbit state over a specific point. The derivation procedure is similar to Controller 1, with a few additional considerations due to the nature of the Milankovitch elements. For this controller, we only target the slow variables and free the fast variable, which in this case would be the true longitude. The error state can be defined as follows:

$$\delta\boldsymbol{x}_{\text{slow}} = \boldsymbol{x}_{\text{slow}} - \boldsymbol{x}^*_{\text{slow}} \tag{39}$$

Where the slow state can be written as follows:

$$\boldsymbol{x}_{\text{slow}} = \begin{bmatrix} a & e & i & \Omega & \omega & M \end{bmatrix}^\top \tag{40}$$

Furthermore, this leads us to the result that the slow state time derivative is a $0_{5\times1}$ vector. Next, considering a candidate Lyapunov function as follows:

$$V = \delta\boldsymbol{x}_{\text{slow}}^\top K \delta\boldsymbol{x}_{\text{slow}} \tag{41}$$

Where $K \in \mathbb{R}^{5\times5}$ and is positive definite. Therefore, the Lyapunov rate is:

$$\dot{V} = 2\delta\boldsymbol{x}_{\text{slow}}^\top K \delta\dot{\boldsymbol{x}}_{\text{slow}} \tag{42}$$

The rest of the derivation is mostly identical to Controller 1. There are a few differences, such as $\boldsymbol{x}$ being replaced by $\boldsymbol{x}_{\text{slow}}$ and $\dot{\boldsymbol{x}}_{\text{slow}} = B_{\text{slow}}\boldsymbol{u}$. This simplification is made possible since the time derivative of the slow variables is $\boldsymbol{f}_{0,\text{slow}} \approx 0$ with minor deviations occurring due to SRP and solar gravity perturbations. Furthermore, to get the desired stabilizing controller, we set the Lyapunov rate to a negative simple Lyapunov candidate function, similar to Controller 1. Then, we get the following derivation:

$$\delta\boldsymbol{x}^\top((1+\omega P)K + \omega(\tfrac{1}{2}K\delta\boldsymbol{x})\tfrac{\mathrm{d}P}{\mathrm{d}g}\tfrac{\mathrm{d}g}{\mathrm{d}\boldsymbol{x}})(\boldsymbol{f}_0 + B\boldsymbol{u})) = -\delta\boldsymbol{x}^\top Q\delta\boldsymbol{x} \tag{43}$$

Where Q is assumed to be of the form $I_{5\times5}$ and positive definite. For compact expression, define the following:

$$L = \left[2(1+wP)K + wK\delta\boldsymbol{x}_{\text{slow}}\frac{\partial P}{\partial g}\frac{\partial g}{\partial \boldsymbol{x}_{\text{slow}}}\right]B_{\text{slow}}$$

This may be expanded to consider multiple penalty functions in the following form:

$$L = (2(1+\sum\omega_i\dot{P}_i)K + (K\delta\boldsymbol{x})\sum\omega_i\frac{\mathrm{d}P_i}{\mathrm{d}g_i}\frac{\mathrm{d}g_i}{\mathrm{d}\boldsymbol{x}}) \tag{44}$$

Where $L \in \mathbb{R}^{5\times3}$ and assumed to be full. Lastly, Solve for the control u by using a pseudo-inverse since L is not square:

$$\boldsymbol{u} = -\left(L^\top L\right)^{-1}L^\top\delta\boldsymbol{x}_{\text{slow}} \tag{45}$$

Using similar form as controller 1 for the penalty functions, we now redefine them in Milankovitch element form. Start with the minimum radius constraint using parameters, $r_{\min}$, weight ω_1 and sharpness k_1.

$$g_1(\boldsymbol{x}_{\text{slow}}) = r_{\min}^2 - \frac{h^2/\mu}{1+e} \tag{46}$$

$$\frac{dg_1(\boldsymbol{x}_{\text{slow}})}{d\boldsymbol{x}_{\text{slow}}} = \begin{bmatrix} -\frac{(2\boldsymbol{h}_1+\boldsymbol{h}_2^2+\boldsymbol{h}_3^2)}{\mu}\frac{1}{1-e} \\ -\frac{(2\boldsymbol{h}_2+\boldsymbol{h}_1^2+\boldsymbol{h}_3^2)}{\mu}\frac{1}{1-e} \\ -\frac{(2\boldsymbol{h}_3+\boldsymbol{h}_2^2+\boldsymbol{h}_1^2)}{\mu}\frac{1}{1-e} \\ -\frac{\boldsymbol{e}_1h^2}{\mu e(e-1)^2} \\ -\frac{\boldsymbol{e}_2h^2}{\mu e(e-1)^2} \\ -\frac{\boldsymbol{e}_3h^2}{\mu e(e-1)^2} \end{bmatrix} \tag{47}$$

Next, formulate the maximum radius constraint, $r_{\max}$, weight ω_2 and sharpness k_2.

$$g_2(\boldsymbol{x}_{\text{slow}}) = \frac{h^2/\mu}{1+e} - r_{\max}^2 \tag{48}$$

$$\frac{dg_2(\boldsymbol{x}_{\text{slow}})}{d\boldsymbol{x}_{\text{slow}}} = \begin{bmatrix} -\frac{(2\boldsymbol{h}_1+\boldsymbol{h}_2^2+\boldsymbol{h}_3^2)}{\mu}\frac{1}{1-e} \\ -\frac{(2\boldsymbol{h}_2+\boldsymbol{h}_1^2+\boldsymbol{h}_3^2)}{\mu}\frac{1}{1-e} \\ -\frac{(2\boldsymbol{h}_3+\boldsymbol{h}_2^2+\boldsymbol{h}_1^2)}{\mu}\frac{1}{1-e} \\ -\frac{\boldsymbol{e}_1h^2}{\mu e(e-1)^2} \\ -\frac{\boldsymbol{e}_2h^2}{\mu e(e-1)^2} \\ -\frac{\boldsymbol{e}_3h^2}{\mu e(e-1)^2} \end{bmatrix} \tag{49}$$

Lastly, derive the cone constraint along the x-axis with half angle α, weight ω_3 and sharpness k_3.

$$g_3(\boldsymbol{x}) = \cos(\frac{\pi}{2}+\alpha) - (\frac{h_1}{h}) \tag{50}$$

$$\frac{dg_3(\boldsymbol{x}_{\text{slow}})}{d\boldsymbol{x}_{\text{slow}}} = \begin{bmatrix} \frac{\boldsymbol{h}_2^2+\boldsymbol{h}_3^2}{h^{1.5}} \\ -\frac{\boldsymbol{h}_1\boldsymbol{h}_2}{h^{1.5}} \\ -\frac{\boldsymbol{h}_1\boldsymbol{h}_3}{h^{1.5}} \\ 0 \\ 0 \\ 0 \end{bmatrix} \tag{51}$$

These penalty functions are then incorporated into the controller derived earlier to impose the path constraints.

5 OpNav and EKF Performance Analysis.

To start, a simplified base case is used by choosing the asteroid Bennu for which abundant information is available. This is ideal for testing and tuning the filter as simulated 'truth' and filter predictions can be validated. The relevant initial conditions and properties used are shown in Table 1, where M is the mass of the asteroid, e is the eccentricity of the asteroid's orbit and r is the mean radius of the asteroid.
[2, 26]

Parameter	Value
M	$7.329 \times 10^{11}\,\text{kg}$
μ	$4.8904 \times 10^{-9}\,\text{km}^3/\text{s}^2$
μ_{Sun}	$132712 \times 10^{6}\,\text{km}^3/\text{s}^2$
G_1	$1 \times 10^{8}\,\text{kg.km}^3/(\text{s}^2.\text{m}^2)$
B	33
a	168505699.04945242405 km
e	0.2037450762416414
d	$1.72 \times 10^{8}\,\text{km}$
r	0.241 km

Table 1. Dynamical Parameters

Additionally, the OpNav parameters used for this research are shown in table 2.

Parameter	Value
θ_{FOV}	90°
S	1000 pixels
α	0
dx	1
dy	1

Table 2. OpNav Parameters

5.1 Distance and Angle Accuracy Analysis. The OpNav algorithm's accuracy at varying distances and lighting conditions is examined by running multiple simulations with noise at varied fixed points.

In the case of distance, 10 test cases are run at each distance at increments of 1 km starting from 1 km upto 30 km. A side-on view where exactly half of the body is lit is used for consistency to fix the angle at a value where the OpNav algorithm is known to be accurate.

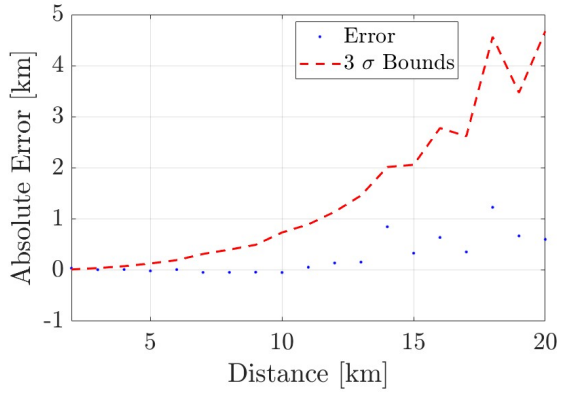

Figure 3. OpNav Error Variation over Distance

As can be seen in Fig. 3, the OpNav algorithm is highly effective at low range, but starts to involve major error at distances greater than 25-30 times the radius of the asteroid. In this case we can see that deviation becomes visibly significant after a distance of around 10 km. However, the analytical covariance still provides a good envelop of the errors. We can define one range observability constraint based on this result. While OpNav does still provide results beyond this, eventually the magnitude of the error exceeds the absolute value of the distance itself, which makes it unusable after a certain point. Therefore, the algorithm must be used within this range, which has now been successfully determined. This distance is still a greater capability than near-range observation methods which require the spacecraft to be much closer than 25-30 times the asteroid radius.

In the case of lighting conditions, 5 test cases are run at each angle at increments of 15 degrees starting from -90 degrees (straight-on or full moon) upto +90 degrees (dark-side or new moon), where 0 degrees is aligned with the side-on view. These are done with a fixed distance of 5 km for consistency and at a range where the OpNav algorithm is accurate.

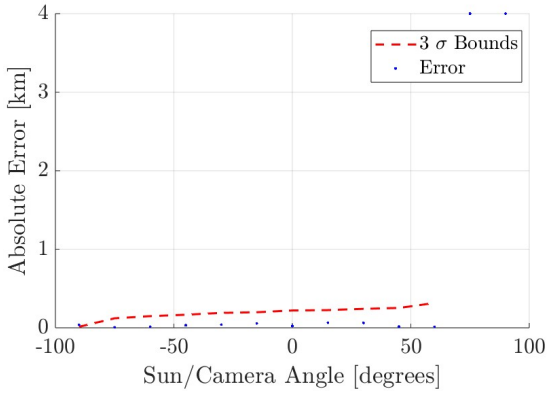

Figure 4. OpNav Error Variation over Angle

We can infer from the graphed results that the algorithm is accurate for most angles except straight-on due to the terminator effect, as well as angles close to the dark side as the size of the lit horizon shrinks. The performance deteriorates if the spacecraft is viewing the asteroid from within 30 degrees of the x axis near the dark side. The covariance is undefined when viewing the dark side as there are no horizon points detected. The error is accordingly equivalent to the true distance of the spacecraft in the implementation used for this research, as the OpNav algorithm returns a zero measurement due to an absence of input horizon points. In other words, the measurement is unusable in these lighting conditions. From this experiment, we define a keep-out cone to ensure the observability, which is given as a cone with a 30 degree half angle along the x-axis.

5.2 OpNav Elliptic Shape Performance. We now test the OpNav performance against increasingly elliptical bodies. As can be seen in Fig. 5, the OpNav error and covariance increase considerably with highly elliptic bodies. While it is still valid up to an ellipsoid with shape ratio 3:1, its performance may be unsatisfactory for any bodies significantly more elliptical. There is potential for improvement on the OpNav algorithm's effectiveness in such situations. For this testcase, we simulate along one revolution of an FTO with a radius of 2.0429km.

5.3 Trajectory Testing. The OpNav algorithm and EKF are tested across various types of trajectories, such as hyperbolic approaches and flybys, distant encirclements, unique orbits and more to ascertain properties of its performance across various situations and deduce when it is more effective or may have room for further improvement.

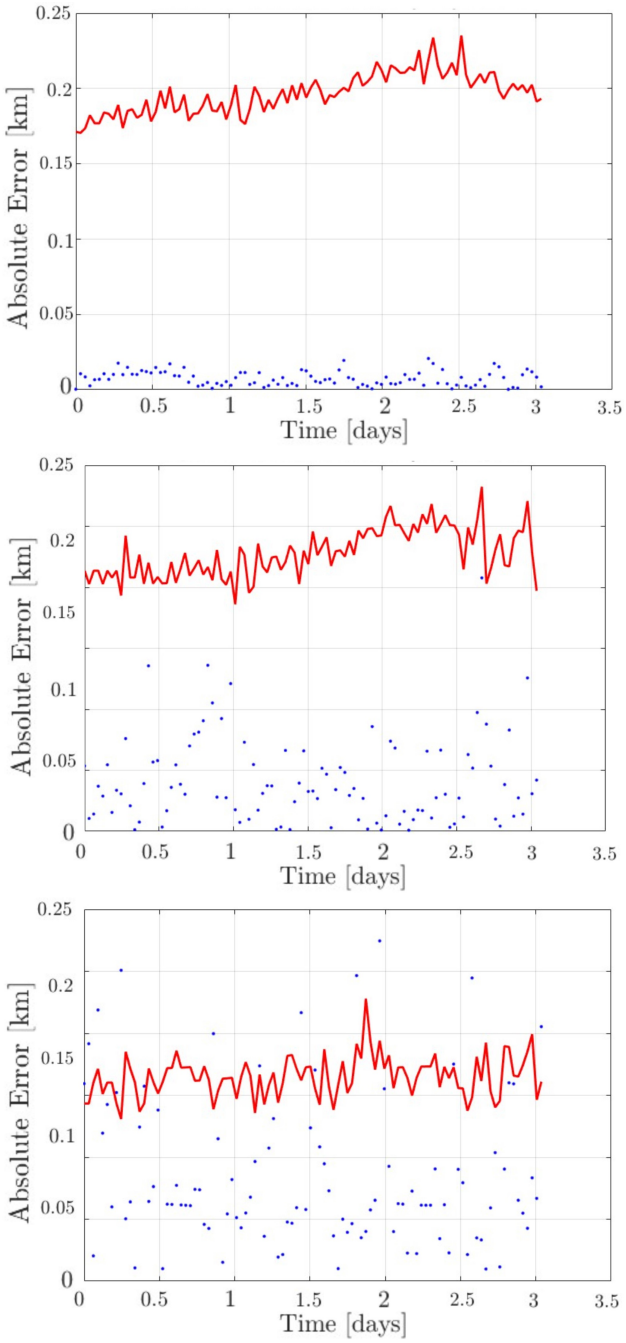

Figure 5. OpNav Error Plots for Sphere, [3 1 1] and [5 1 1] Ellipsoid

These initial conditions are arbitrarily chosen in terms of both position and velocity to provide some variation and generate natural paths that a spacecraft may follow depending upon its nature of approach to an asteroid. A few sample results can be seen in Fig. 6. The first case depicted a hyperbolic flyby from a large distance. The second test is conducted at a medium range, keeping a similar distance from the asteroid while changing the lighting condition. The last case demonstrates another flyby where the asteroid is approached closely and the spacecraft passes through the dark side. These demonstrate the EKF's ability to smoothen the predicted state and match the true trajectory once the spacecraft is within range for effective OpNav measurements. However, it diverges at large distances.

Based on this behaviour, we can infer that when approaching near-linearly from the same angle, position estimation is best. For highly ellipsoidal cases, when angle varies extremely or highly nonlinear trajectory, horizon-based OpNav, and hence EKF, become inaccurate. For near-spherical cases, OpNav seems to work accurately at all times. OpNav is ideal for medium range when in hyperbolic trajectory, before view angle starts changing rapidly (before/after view point). The state estimates become inaccurate at large distances (greater than 25-30x mean radius).

6 Numerical Results.

6.1 Orbit Maintenance Scenario. In order to simulate the application of the Lyapunov controller in a realistic scenario, we implemented it in a loop such that the Lyapunov controller computes each successive timestep based on the EKF's prediction, rather than using the true position. The true state is then updated using the control calculated by the controller, from which the OpNav measurement is taken at a realistic frequency of every 1.5 hours and provided to the EKF for the next prediction. This means that any significant error in the EKF's position estimate for the spacecraft could lead to complete divergence of the true and estimated states. Hence, it is critical for the measurements to be continuously reliable.

To demonstrate the effectiveness of the observability enhancing controller, we develop a test scenario where a spacecraft starts with an arbitrary initial condition on a trajectory to flyby passing behind the dark side of Bennu. The target is a circular orbit with an inclination just above 30 degrees. This avoids the dark-side cone but provides a useful edge case to test where the spacecraft may often travel through the poor observability region in its controlled trajectory without an observability penalty. The initial conditions in cartesian terms are $r = [1.0214, 0, -2.0429]$ km and $v = [40.493, 40.493, 40.493]$ mm/s. The gain is updated to an order of magnitude lower and found to provide better performance given the proximity to the asteroid.

$$K_{2.1} = \begin{bmatrix} 10^{-2} & 0 & 0 & 0 & 0 & 0 \\ 0 & 10^{-3} & 0 & 0 & 0 & 0 \\ 0 & 0 & 10^{-3} & 0 & 0 & 0 \\ 0 & 0 & 0 & 10^{-4} & 0 & 0 \\ 0 & 0 & 0 & 0 & 10^{-3} & 0 \\ 0 & 0 & 0 & 0 & 0 & 10^{-4} \end{bmatrix} \tag{52}$$

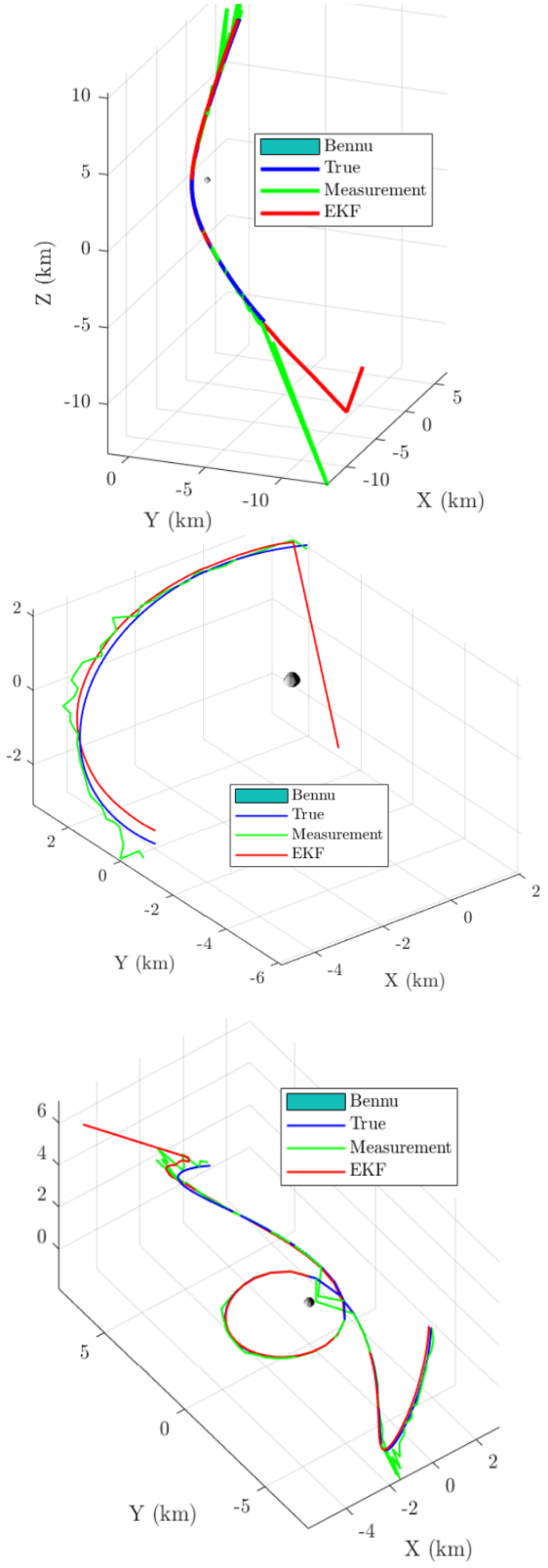

Figure 6. Sample OpNav Testing Trajectories

For this case, the following initial covariance is used (covariances for position in $\left[\text{km}^2\right]$ and velocity in $\left[\frac{\text{km}^2}{\text{s}^2}\right]$):

$$P_0 = \begin{bmatrix} 3.2761 & 0 & 0 & 0 & 0 & 0 \\ 0 & 3.2761 & 0 & 0 & 0 & 0 \\ 0 & 0 & 3.2761 & 0 & 0 & 0 \\ 0 & 0 & 0 & 8.544 \times 10^{-17} & 0 & 0 \\ 0 & 0 & 0 & 0 & 8.544 \times 10^{-17} & 0 \\ 0 & 0 & 0 & 0 & 0 & 8.544 \times 10^{-17} \end{bmatrix} \tag{53}$$

To compare results, we begin by testing the Lyapunov controller without the observability improving penalty functions as shown in Fig. 7. A few camera snapshots with the detected horizon points highlighted in red can be seen in Fig. 8. As can be seen in the results for the controller without an observability penalty, the spacecraft travels through the poor observability region near the dark side of the asteroid. This leads to a faulty measurement characterized by the spike in the OpNav measurement history. This is used by the EKF, causing the true and estimated trajectories to diverge.

We now compare this performance to that of the observability enhancing controller in Fig. 9. A few camera snapshots with the detected horizon points highlighted in red can be seen in Fig. 10. In the observability enhancing case, the controller successfully avoids the poor observability region, as can be seen by the consistent matching of the OpNav measurement and EKF prediction to the true trajectory at all times.

Monte Carlo Analysis To demonstrate the robustness of the algorithm, a monte carlo analysis is conducted to perform a statistical analysis of its success rate. A realistic initial standard deviation is defined for the position error across each direction (x, y and z) of $\sigma = 30$ meters, approximately 10% of the asteroid Bennu's radius. This is used to apply an initial error to the true initial state to generate the EKF's initial known state. The simulation is run for 20 iterations. To start, we test the version without observability enhancement in order to understand the severity of failures in this scenario. As per the results in Fig. 11, the Lyapunov controller fails in every case without the observability enhancement, as it passes through the poor observability region in every test. The EKF and true dynamics diverge completely and lead to the spacecraft either crashing into the asteroid or travelling out of the system. Now, we compare this with the observability enhancing case in Fig. 12. The observability enhancing Lyapunov controller shows better performance and success rate of the spacecraft reaching its desired orbit. It succeeds in 18 out of 20 iterations. This is a major improvement in performance, and supports the utility of the observability enhancing controller.

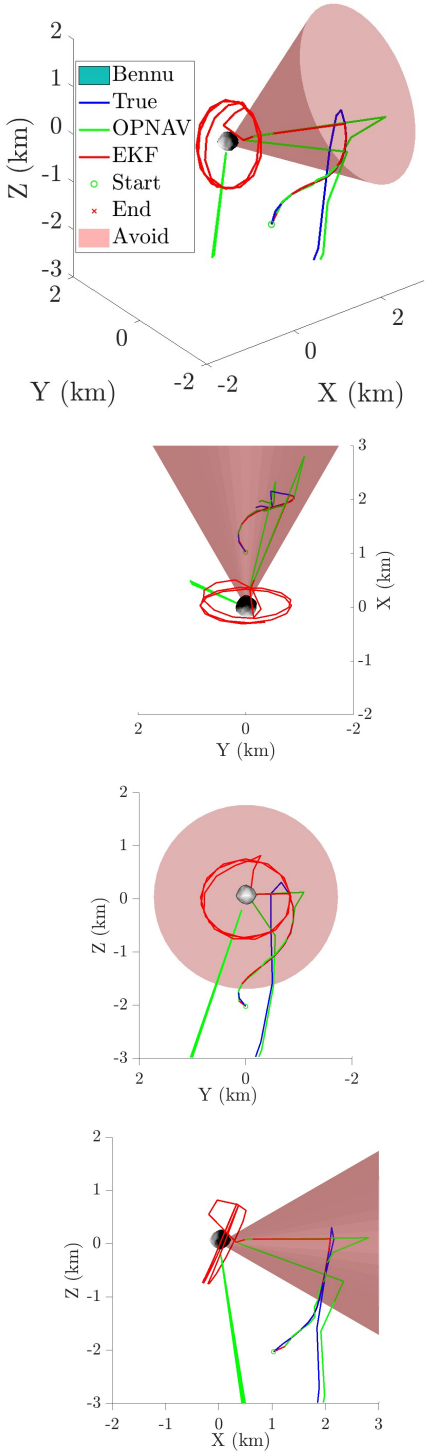

Figure 7. True, OpNav and EKF Trajectories Without Observability Enhancing Penalty Lyapunov Control around Bennu shown in 4 views

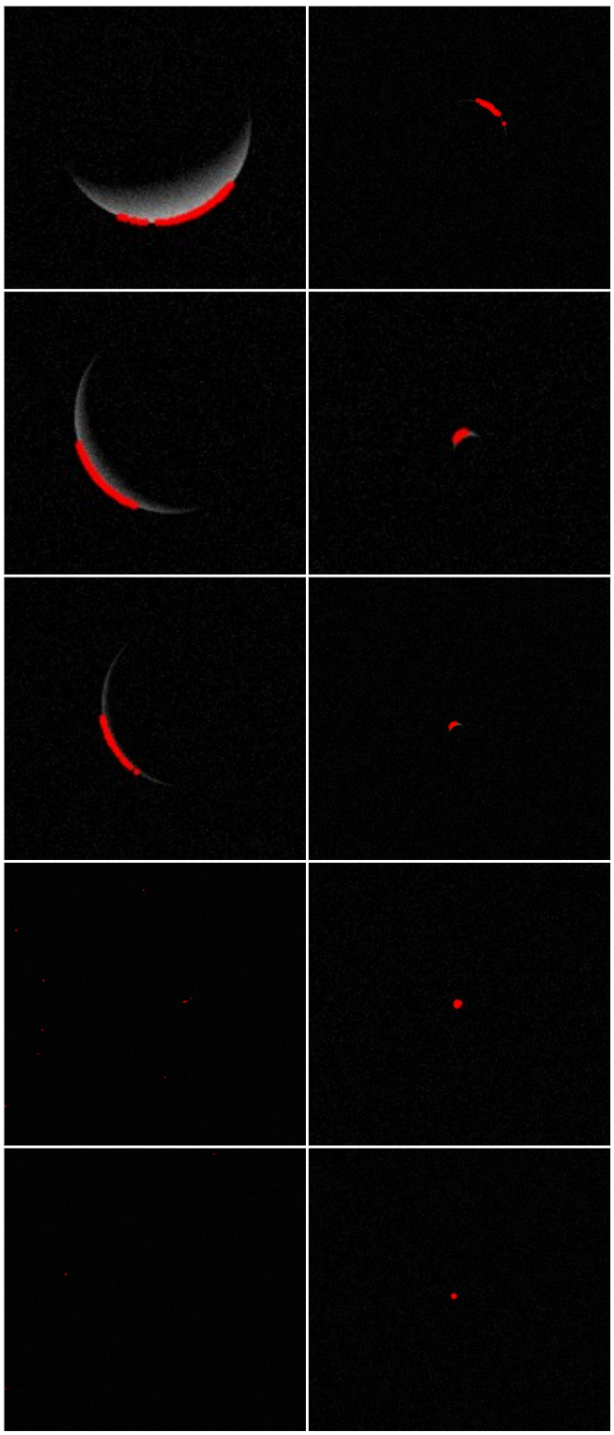

Figure 8. Sample Image History with Detected Horizon Points from Fig. 7 for Case Without Observability Enhancement

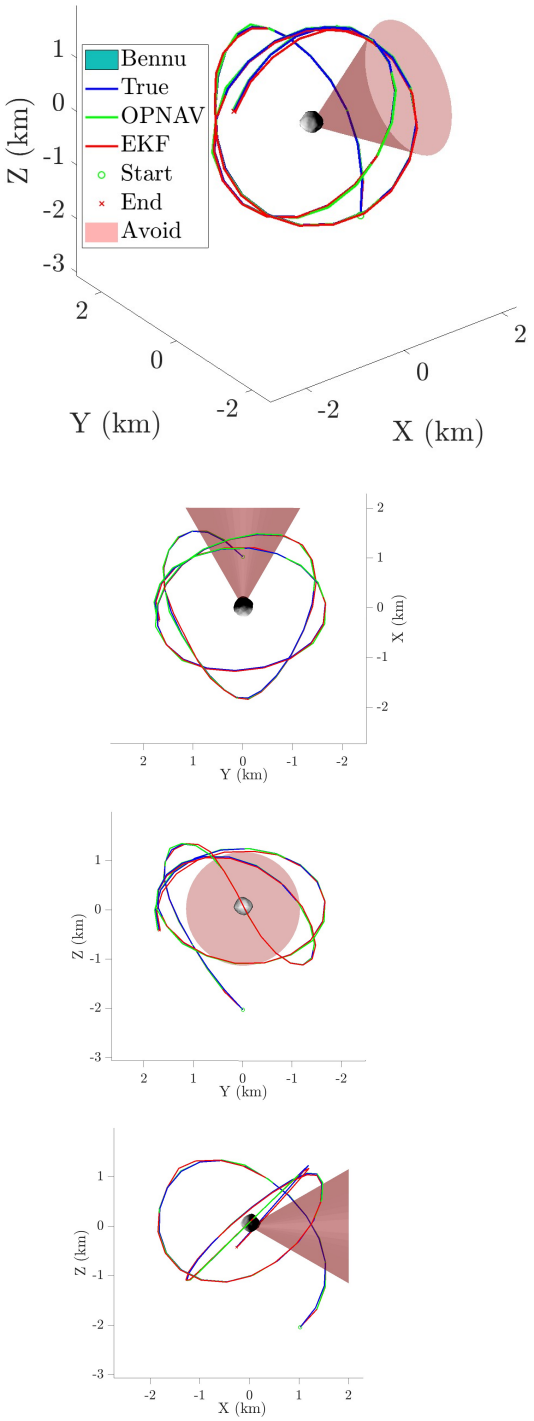

Figure 9. True, OpNav and EKF Trajectories With Observability Enhancing Penalty Lyapunov Control around Bennu shown in 4 views

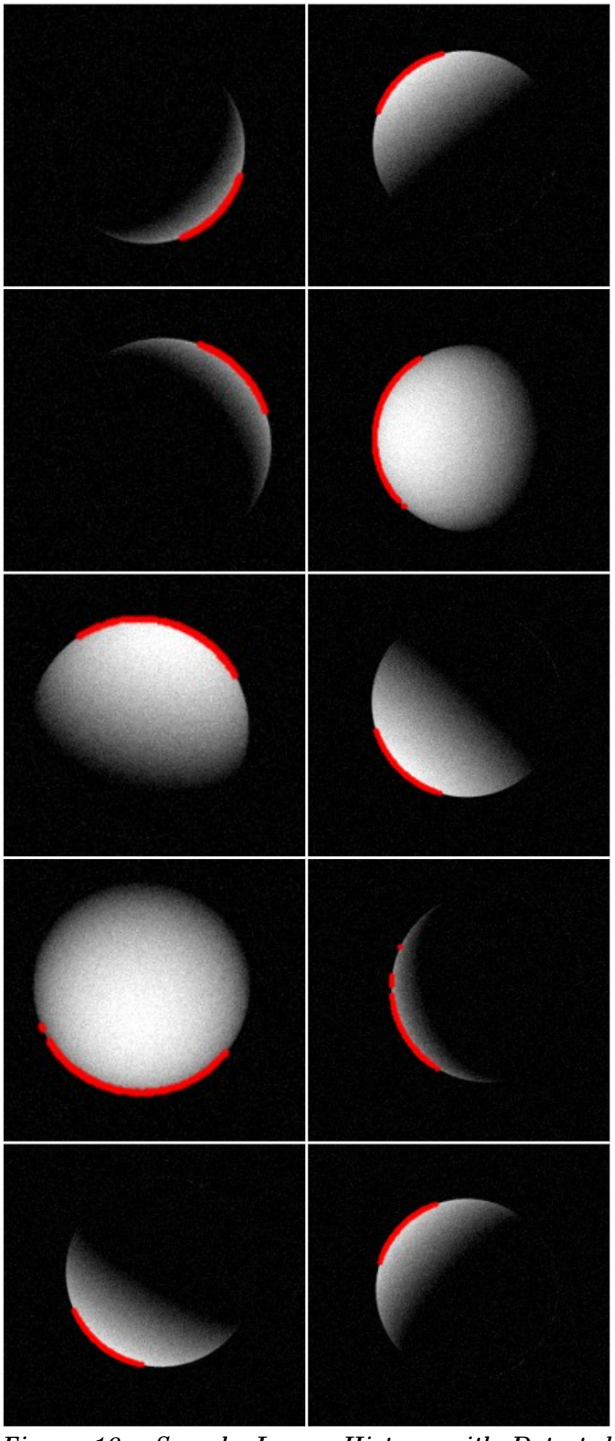

Figure 10. Sample Image History with Detected Horizon Points from Fig. 9 for Case With Observability Enhancement

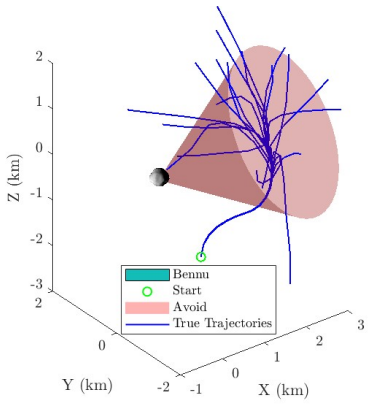

Figure 11. Monte Carlo Simulation of 20 True Trajectories using Basic Lyapunov Controller

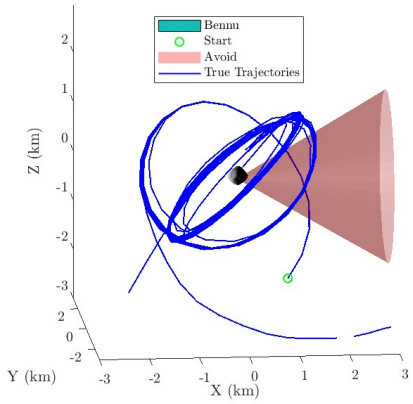

Figure 12. Monte Carlo Simulation of 20 True Trajectories using Observability Enhancing Lyapunov Controller

6.2 Approach and Capture Scenario. Beyond the orbit maintenance scenario, it is important to demonstrate the effectiveness of this controller in a greater variety of situations, including those starting further away from the asteroid. Therefore, we tested this algorithm in a specific testcase where we start by targeting the asteroid using the phase 1 controller and switch over to the phase 2 controller once the spacecraft is within 10 asteroid radii. At this point, the controller targets a frozen terminator orbit very near the surface of the asteroid, first getting into the correct plane and then reducing the semi major axis. For this case, the following initial covariance is used (position covariances in $\left[\text{km}^2\right]$ and velocity covariances in $\left[\frac{\text{km}^2}{\text{s}^2}\right]$):

$$P_0 = \begin{bmatrix} 3.2761 & 0 & 0 & 0 & 0 & 0 \\ 0 & 3.2761 & 0 & 0 & 0 & 0 \\ 0 & 0 & 3.2761 & 0 & 0 & 0 \\ 0 & 0 & 0 & 8.544 \times 10^{-12} & 0 & 0 \\ 0 & 0 & 0 & 0 & 8.544 \times 10^{-12} & 0 \\ 0 & 0 & 0 & 0 & 0 & 8.544 \times 10^{-12} \end{bmatrix} \tag{54}$$

The gains found to return best performance for controller phase 1 in this particular testcase is $K_1 = 0.01 I_{6\times 6}$ for controller 1. Additionally, the penalty function parameters used are $r_{\min} = 2 \times R_{\text{asteroid}}$, $\omega_1 = 1$ and $k_1 = 1$ for the minimum radius constraint $r_{\max} = 25 \times R_{\text{asteroid}}$, $\omega_2 = 1$ and $k_2 = 1$ for the maximum radius constraint and $\alpha = 30\,\text{deg}$, $\omega_3 = 1$ and $k_3 = 1$ for the cone constraint.

For controller 2, there are two sets of gains used, which are tuned and determined experimentally. First, one that is ideal to transfer to the plane of the FTO but not necessarily attain the desired semi major axis. Second, one that is ideal to transfer from any circular orbit in the FTO plane to the desired FTO orbit. The chosen gains are as follows:

Gain 2.1 for transferring from any incoming state from the stage 1 controller to the FTO plane:

$$K_{2.1} = \begin{bmatrix} 10^{-2} & 0 & 0 & 0 & 0 & 0 \\ 0 & 10^{-3} & 0 & 0 & 0 & 0 \\ 0 & 0 & 10^{-3} & 0 & 0 & 0 \\ 0 & 0 & 0 & 10^{-4} & 0 & 0 \\ 0 & 0 & 0 & 0 & 10^{-3} & 0 \\ 0 & 0 & 0 & 0 & 0 & 10^{-4} \end{bmatrix} \tag{55}$$

Gain 2.2 for transferring between current FTO to desired FTO:

$$K_{2.2} = \begin{bmatrix} 10^{-3} & 0 & 0 & 0 & 0 & 0 \\ 0 & 10^{-3} & 0 & 0 & 0 & 0 \\ 0 & 0 & 10^{-3} & 0 & 0 & 0 \\ 0 & 0 & 0 & 10^{-3} & 0 & 0 \\ 0 & 0 & 0 & 0 & 10^{-6} & 0 \\ 0 & 0 & 0 & 0 & 0 & 10^{-6} \end{bmatrix} \tag{56}$$

The penalty function parameters chosen for controller 2 are identical to that for controller 1, except the weight for the cone constraint is increased to $\omega_3 = 10$. This leads to better performance in terms of avoiding the poor observability region at a closer proximity to the asteroid. The complete trajectory is shown in Fig. 13.

Based on the results, we can see that the overall controller is successful. It approaches the asteroid with a low control input where the control profile only seems to diverge because it is a very small, precise and continuous adjustment that is cut off before reaching the target. It then switches to the FTO transfer controller which correctly changes and maintains the desired plane with minimal and quick control input. Lastly it transfers to the final desired FTO using some small final adjustments. In terms of observability, which is the primary goal, the controller does maintain a trajectory within the minimum and maximum radii to avoid intersecting the asteroid or straying too far. Additionally, in Fig. 14, we can see that the controller does adjust the spacecraft's trajectory to avoid entering the keep-out cone which would lead to a viewing angle too close to the dark side. Therefore, it is improving observability which would normally lead to an erroneous result without control.

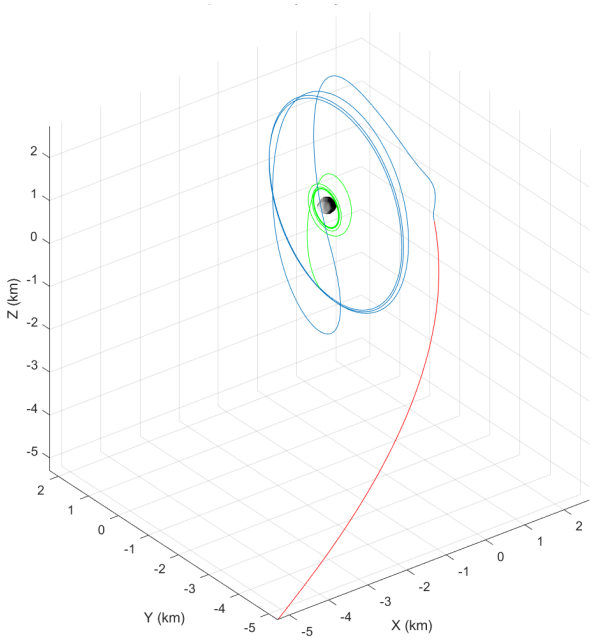

Figure 13. Controlled Spacecraft trajectory around Bennu, Diagonal view

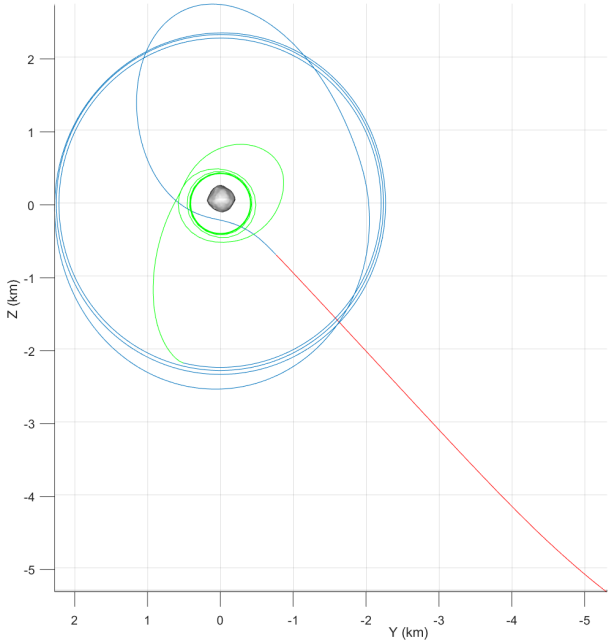

Figure 14. Controlled Spacecraft trajectory around Bennu, Straight-on view

We then compared the regular and observability enhancing controllers in this scenario, then applied OpNav and state estimation using the EKF along the generated trajectory. Note that in this method, the Lyapunov controller is not reliant on the state estimate, but rather used to generate the full trajectory upon which the rest of the algorithm is tested. However, the intent is to test this case to the same degree as the orbit maintenance scenario in future developments on this topic. These results are shown in Fig. 15.

Next, a monte carlo analysis is conducted for 20 iterations using an initial standard deviation of the position error across each direction (x, y and z) of $\sigma = 0.2$ kilometers. This is approximately 100% of the asteroid Bennu's radius and is used to apply an initial error to the true initial state to generate the EKF's initial known state. It is set to a higher value to more rigorously test the EKF robustness since it follows a predetermined true trajectory in this case. This is different from the orbit maintenance scenario where the true trajectory was dependent on the Lyapunov control derived from EKF state estimates. As seen in Fig. 16, there is a clear spike in error when the spacecraft passes through the poor observability region in every test while using the original version of the controller without path constraints. Meanwhile, as seen in Fig. 17 the path constrained controller successfully reduces this error on every iteration. This supports the robustness of the controller in this scenario.

7 Discussion. This paper presents a promising approach to autonomous asteroid OpNav using a Lyapunov controller with path constraints for observability-enhancing maneuvers. The approach offers a combination of OpNav methods, state estimation and control, especially in the context of navigating the challenging environments around asteroids.

One of the major challenges identified is the limited applicability of the OpNav algorithm under extreme lighting conditions, such as when the spacecraft is positioned behind the dark side of the asteroid. This creates poor observability for the system due to an undetectable horizon, potentially leading to inaccurate state estimations. The observability enhancing controller concept allows the design of a control scheme that ensures a spacecraft follows a trajectory that avoids these faulty measurements. This is a better method than simply discarding poor measurements, as that may lead to an extended gap without a reference, causing the state estimate to diverge. This research also develops understanding of the applicability of horizon-based OpNav as a measurement for asteroid navigation. It is found that it is effective up to a range of 25-30 times a target asteroid's radius, outside of a cone with a 30 degree half angle from either straight-on or dark-side viewing and displays reasonable performance with an ellipsoidal target body upto a 3:1 shape axis ratio.

The EKF, while effective under certain conditions, shows divergence in scenarios with extreme noise, highly nonlinear dynamics, or erroneous initial states. This highlights the need for further tuning and refinement of the EKF's robustness. However, it is effective within

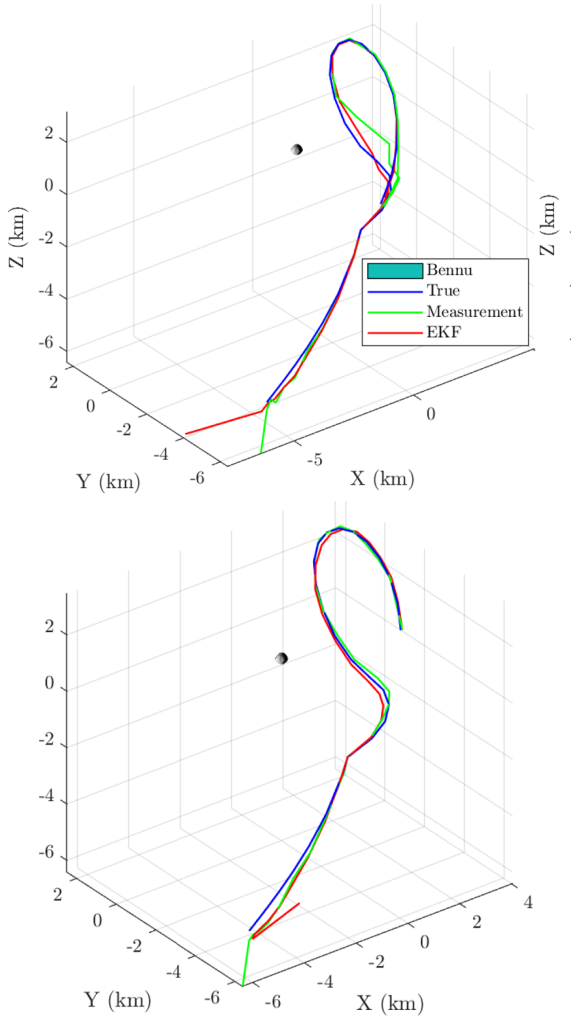

Figure 15. Controlled trajectory without (T) and with (B) Observability-improving penalty and EKF performance

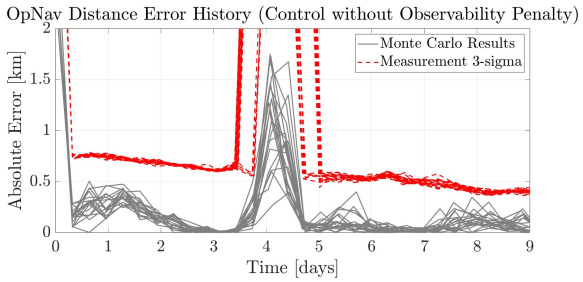

Figure 16. OpNav position error monte carlo with varied initial position for control without observability penalty ($\sigma = 0.2$ km)

realistic bounds and expectations of these parameters that would be found in an actual space mission. The system demonstrates effective state estimation for spherical bodies and near-stable orbits, but performance deteriorates with more complex, nonlinear trajectories

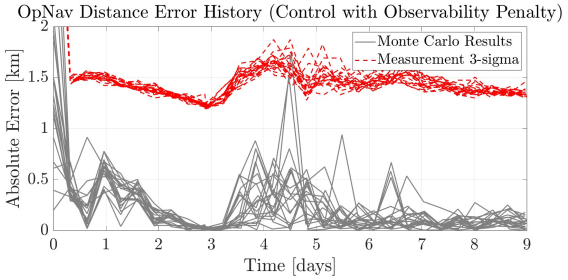

Figure 17. OpNav position error monte carlo with varied initial position for control with observability penalty ($\sigma = 0.2$ km)

or highly elliptical asteroids. This indicates a need for improvements to the algorithm that can handle irregular bodies. This is explained by the fact that the current model does not yet provide sufficient observability for shape estimation, particularly when attempting to estimate the radius or shape ratios of the asteroid. More information is required for the filter to successfully estimate these parameters. Two options to do so are through additional optical methods to infer properties such as the asteroid's triaxial ellipsoid shape ratios and differential imaging to determine velocity in order to make the system observable in terms of shape estimation. We are currently investigating these methods as the next step in the algorithm's development.

While the image generation method used for this research is quick, generating each image at an average rate of 0.3 seconds, it is still the computational restriction for the numerical simulation. However, it would be useful to conduct a comparative accuracy and computation cost study between the accuracy of these images to existing synthetic image generators to determine its reliability as a basis to test the Lyapunov controller on.

The current approach to trajectory generation through Lyapunov control has shown significant improvements, but it is important to test it against a wider range of scenarios with varying tuning parameters to determine a more intuitive approach to adapting the controller to any desired mission profile. Formulating an objective function that analytically quantifies observability within the Lyapunov controller rather than using a path constraint could lead to even more robust and stable performance. An additional avenue for investigation is the OpNav measurement interval and how it may affect the controller's success rate. This may create a baseline to design the spacecraft sensor such that it may balance measurement cost and state estimate accuracy. Additionally, the gain must be very precisely tuned as asteroid environment requires precise control. It is very sensitive and therefore highly susceptible to minor changes in the gain or control profile. Potential improvements to improve the algorithm include its

adaptability to more elliptical asteroid bodies, refining controller gain settings for different mission profiles, and exploring additional optical methods to enhance shape and state estimation simultaneously.

This method of using a horizon-based OpNav with observability enhancing Lyapunov Control may offer a more computationally efficient and autonomous option for the early mission approach phase. It reduces the need of human-in-the-loop OpNav since the spacecraft has the ability to navigate itself to attain useful measurements as it approaches the asteroid. Furthermore, it has computation efficiency and accuracy advantages over other OpNav methods for a wider range of observable distances and angles. For example, while the natural feature tracking offers better accuracy, this is applicable at closer range, in lighting conditions where the surface is visible and requires more computation time. Meanwhile, LOS is limited in its accuracy compared to the horizon-based method. However, the horizon-based OpNav performance may be limited for highly elliptical bodies. Lastly, it is important to note that this method to use horizon-based OpNav with observability enhanced maneuvers is not intended to fully replace the methodologies used in existing space missions. Rather, we offer an additional method that is feasible to implement to improve mission efficiency and safety. This is because the observability enhancement ensures continuous and reliable measurements at all stages of the mission while within horizon-based OpNav range. Additionally, the Lyapunov Control and state estimation algorithms combined with the OpNav enable autonomy across the early mission approach to close proximity phases of an asteroid mission. There is potential for future work to extend its applicability, improve performance in extreme conditions, and develop more sophisticated state and shape estimation methods. These improvements are critical for expanding the system's use in future deep space exploration missions.

8 Conclusion. This research successfully demonstrates a robust autonomous navigation and control method for spacecraft approaching or conducting operations in the vicinity of asteroids. A comprehensive simulation environment is developed which considers spacecraft dynamics around an asteroid, synthetic asteroid imaging and processing, horizon-based OpNav, EKF, and observability enhancing Lyapunov Control. The novel contributions include the synthetic image generation method which may be used to generate reference images for other optical method tests, and a Lyapunov Controller with path constraints to improve horizon-based OpNav measurement observability. Its effectiveness has been demonstrated by testing its stability when combined with EKF-based state estimation within acceptable error bounds. The validation with Bennu as a realistic benchmark highlights the reliable test of its capabilities in this application. The system's robustness in varying scenarios, including near-linear hyperbolic trajectories, flybys, and various orbit transfers highlights its potential for broader applications in deep space exploration.

9 Appendix A: Controller Gain Tuning Guidelines. Since the gains determined for the controllers for this research are for a specific testcase with Bennu, it is imperative to develop guidelines to derive it for different scenarios to allow it to be used for diverse missions. After investigating the relations between the gains and the controller performance, the following observations and guidelines are made:

1. For the cartesian version of the Lyapunov controller, the gain $K_1 = 0.01I_{6\times6}$ is used. Each axis is assigned an equivalent gain in this case as each of them exhibit identical significance to the control profile. This value sets the magnitude of the gain in each axes to the order of magnitude of the spacecraft's nondimensional position, which would vary depending on the system, trajectory and primary body. This is a good starting point to tune the gain and can be tweaked to be higher or lower depending on the desired type of performance (e.g. underdamped, critically damped or overdamped).

2. For the milankovitch version of the Lyapunov controller, the base value used is found to be a gain of 10^{-3} where the gains in the angular momentum vector and eccentricity vector are tweaked to a different ratio across varying axes depending on in which direction the control is intended to be imparted. This value seems to offer a critical balance and match with a few orders of magnitude below the values of angular momentum and eccentricity used in this research, allowing precise changes. The eccentricity gains never exceed the angular momentum, as this is found to create unstable results.

3. The first gain is used to transfer from any arbitrary incoming state to the FTO plane. Here, the angular momentum in the x direction has a higher gain, and the eccentricity in the x and y directions have lower gains. The intuition is that this allows the controller to readily tweak the spacecraft's position and counter the effect of SRP. For a different application where the dynamics is more balanced, this distinction in gain may not be required.

4. The second gain is used to transfer between FTOs. Here, the eccentricity in the y and z direction is set to a lower gain, which allows the controller to rapidly adjust those parameters to attain a different altitude while maintaining the spacecraft in the FTO plane. Depending on the nature of the mission and target

orbit, different axes can have modified gains to execute transfers within a desired plane.

Using these observations, this Lyapunov controller formulation may be adapted for different use cases. Results demonstrating the effectiveness of these gains can be seen in section 6.2.

References.

[1] T. Yada, M. Abe, T. Okada, A. Nakato, K. Yogata, A. Miyazaki, K. Hatakeda, K. Kumagai, M. Nishimura, Y. Hitomi, H. Soejima, M. Yoshitake, A. Iwamae, S. Furuya, M. Uesugi, Y. Karouji, T. Usui, T. Hayashi, D. Yamamoto, R. Fukai, S. Sugita, Y. Cho, K. Yumoto, Y. Yabe, J. P. Bibring, C. Pilorget, V. Hamm, R. Brunetto, L. Riu, L. Lourit, D. Loizeau, G. Lequertier, A. Moussi-Soffys, S. Tachibana, H. Sawada, R. Okazaki, Y. Takano, K. Sakamoto, Y. N. Miura, H. Yano, T. R. Ireland, T. Yamada, M. Fujimoto, K. Kitazato, N. Namiki, M. Arakawa, N. Hirata, H. Yurimoto, T. Nakamura, T. Noguchi, H. Yabuta, H. Naraoka, M. Ito, E. Nakamura, K. Uesugi, K. Kobayashi, T. Michikami, H. Kikuchi, N. Hirata, Y. Ishihara, K. Matsumoto, H. Noda, R. Noguchi, Y. Shimaki, K. Shirai, K. Ogawa, K. Wada, H. Senshu, Y. Yamamoto, T. Morota, R. Honda, C. Honda, Y. Yokota, M. Matsuoka, N. Sakatani, E. Tatsumi, A. Miura, M. Yamada, A. Fujii, C. Hirose, S. Hosoda, H. Ikeda, T. Iwata, S. Kikuchi, Y. Mimasu, O. Mori, N. Ogawa, G. Ono, T. Shimada, S. Soldini, T. Takahashi, Y. Takei, H. Takeuchi, R. Tsukizaki, K. Yoshikawa, F. Terui, S. Nakazawa, S. Tanaka, T. Saiki, M. Yoshikawa, S. ichiro Watanabe, and Y. Tsuda, "Preliminary analysis of the hayabusa2 samples returned from c-type asteroid ryugu," *Nature Astronomy*, vol. 6, 2022.

[2] M. G. Daly, O. S. Barnouin, J. A. Seabrook, J. Roberts, C. Dickinson, K. J. Walsh, E. R. Jawin, E. E. Palmer, R. Gaskell, J. Weirich, T. Haltigin, D. Gaudreau, C. Brunet, G. Cunningham, P. Michel, Y. Zhang, R. L. Ballouz, G. Neumann, M. E. Perry, L. Philpott, M. M. A. Asad, C. L. Johnson, C. D. Adam, J. M. Leonard, J. L. Geeraert, K. Getzandanner, M. C. Nolan, R. T. Daly, E. B. Bierhaus, E. Mazarico, B. Rozitis, A. J. Ryan, D. N. Dellaguistina, B. Rizk, H. C. Susorney, H. L. Enos, and D. S. Lauretta, "Hemispherical differences in the shape and topography of asteroid (101955) bennu," *Science Advances*, vol. 6, 2020.

[3] C. D. Adam, P. G. Antreasian, B. T. Carcich, J. M. Leonard, E. J. Lessac-Chenen, L. K. McCarthy, D. S. Nelson, J. Y. Pelgrift, E. M. Sahr, D. R. Wibben, S. Knutson, H. L. Enos, K. Harshman, C. Hergenrother, J. N. Kidd, D. Lambert, A. T. Polit, B. Rizk, D. S. Lauretta, O. Billett, M. Lefevre, M. C. Moreau, B. J. Bos, A. Calloway, N. Castro, J. Cavaluzzi, K. M. Getzandanner, R. Mink, and D. Poland, "Concept of operations for osiris-rex optical navigation image planning," in *AIAA Science and Technology Forum and Exposition, AIAA SciTech Forum 2022*, 2022.

[4] S. ichiro Watanabe, Y. Tsuda, M. Yoshikawa, S. Tanaka, T. Saiki, and S. Nakazawa, "Hayabusa2 mission overview," 2017.

[5] P. Michel, M. Kueppers, H. Sierks, I. Carnelli, A. F. Cheng, K. Mellab, M. Granvik, A. Kestilä, T. Kohout, K. Muinonen, A. Näsilä, A. Penttila, T. Tikka, P. Tortora, V. Ciarletti, A. Hérique, N. Murdoch, E. Asphaug, A. Rivkin, O. Barnouin, A. C. Bagatin, P. Pravec, D. C. Richardson, S. R. Schwartz, K. Tsiganis, S. Ulamec, and O. Karatekin, "European component of the aida mission to a binary asteroid: Characterization and interpretation of the impact of the dart mission," *Advances in Space Research*, vol. 62, 2018.

[6] H. F. Levison, C. B. Olkin, K. S. Noll, S. Marchi, J. F. Bell, E. Bierhaus, R. Binzel, W. Bottke, D. Britt, M. Brown, M. Buie, P. Christensen, J. Emery, W. Grundy, V. E. Hamilton, C. Howett, S. Mottola, M. Pätzold, D. Reuter, J. Spencer, T. S. Statler, S. A. Stern, J. Sunshine, H. Weaver, and I. Wong, "Lucy mission to the trojan asteroids: Science goals," 2021.

[7] D. C. Qi and K. Oguri, "Analysis of autonomous orbit determination in various near-moon periodic orbits," *Journal of the Astronautical Sciences*, vol. 70, 2023.

[8] X. Ning, M. Gui, J. Fang, Y. Dai, and G. Liu, "A novel differential doppler measurement-aided autonomous celestial navigation method for spacecraft during approach phase," *IEEE Transactions on Aerospace and Electronic Systems*, vol. 53, 2017.

[9] J. A. Christian, "Optical navigation using planet's centroid and apparent diameter in image," *Journal of Guidance, Control, and Dynamics*, vol. 38, 2015.

[10] J. W. McMahon, D. J. Scheeres, and K. Berry, "Asteroid proximity navigation using direct altimetry measurements," in *Advances in the Astronautical Sciences*, vol. 152, 2014.

[11] J. O. Woods and J. A. Christian, "Lidar-based relative navigation with respect to non-cooperative objects," *Acta Astronautica*, vol. 126, 2016.

[12] J. Villa, A. Osmundson, B. Hockman, B. Morrell, D. Lubey, D. Bayard, J. Mcmahon, and I. A. Nesnas, "Light-robust pole-from-silhouette algorithm and visual-hull estimation for autonomous optical navigation to an unknown small body," *AAS GNC Conference*, 2021.

[13] N. Ogawa, F. Terui, Y. Mimasu, K. Yoshikawa, G. Ono, S. Yasuda, K. Matsushima, T. Masuda, H. Hihara, J. Sano, T. Matsuhisa, S. Danno, M. Yamada, Y. Yokota, Y. Takei, T. Saiki, and Y. Tsuda, "Image-based autonomous navigation of hayabusa2 using artificial landmarks: The design and brief in-flight results of the first landing on asteroid ryugu," *Astrodynamics*, vol. 4, 2020.

[14] L. K. McCarthy, C. D. Adam, J. M. Leonard, P. G. Antresian, D. S. Nelson, E. M. Sahr, J. Y. Pelgrift, E. J. Lessac-Chennen, J. L. Geeraert, and D. S. Lauretta, "Osiris-rex landmark optical navigation performance during orbital and close proximity operations at asteroid (101955) bennu," in *AIAA Science and Technology Forum and Exposition, AIAA SciTech Forum 2022*, 2022.

[15] D. Qiao, X. Zhou, Z. Zhao, and T. Qin, "Asteroid approaching orbit optimization considering optical navigation observability," *IEEE Transactions on Aerospace and Electronic Systems*, vol. 58, 2022.

[16] M. Pugliatti, V. Franzese, and F. Topputo, "Data-driven image processing for onboard optical navigation around a binary asteroid," *Journal of Spacecraft and Rockets*, vol. 59, 2022.

[17] H. Jia, S. Zhu, and P. Cui, "Observability-based navigation using optical and radiometric measurements for asteroid proximity," *IEEE Transactions on Aerospace and Electronic Systems*, vol. 56, 2020.

[18] J. A. Christian, "A tutorial on horizon-based optical navigation and attitude determination with space imaging systems," *IEEE Access*, vol. 9, 2021.

[19] R. Furfaro, "Hovering in asteroid dynamical environments using higher-order sliding control," in *Journal of Guidance, Control, and Dynamics*, vol. 38, 2015.

[20] K. W. Lee and S. N. Singh, "Noncertainty-equivalence adaptive attitude control of satellite orbiting around an asteroid," *Acta Astronautica*, vol. 161, 2019.

[21] D. J. Scheeres and F. Marzari, "Spacecraft dynamics in the vicinity of a comet," *Journal of the Astronautical Sciences*, vol. 50, 2003.

[22] D. J. Scheeres, "Orbit mechanics about asteroids and comets," *Journal of Guidance, Control, and Dynamics*, vol. 35, 2012.

[23] J. A. Christian and S. B. Robinson, "Noniterative horizon-based optical navigation by cholesky factorization," in *Journal of Guidance, Control, and Dynamics*, vol. 39, 2016.

[24] J.-J. E. Slotine and W. Li, *Applied Nonlinear Control*. Englewood Cliffs, NJ: Prentice-Hall, 1991.

[25] H. Schaub and J. L. Junkins, *Analytical Mechanics Of Space Systems*. 2003.

[26] P. Tricarico, D. J. Scheeres, A. S. French, J. W. McMahon, D. N. Brack, J. M. Leonard, P. Antreasian, S. R. Chesley, D. Farnocchia, Y. Takahashi, E. M. Mazarico, D. Rowlands, D. Highsmith, K. Getzandanner, M. Moreau, C. L. Johnson, L. Philpott, E. B. Bierhaus, K. J. Walsh, O. S. Barnouin, E. E. Palmer, J. R. Weirich, R. W. Gaskell, M. G. Daly, J. A. Seabrook, M. C. Nolan, and D. S. Lauretta, "Internal rubble properties of asteroid (101955) bennu," *Icarus*, vol. 370, 2021.